AUTOMATIC RECONSTRUCTION OF SHAPE EVOLUTION OF ETFE-FOILS BY CLOSE-RANGE PHOTOGRAMMETRIC IMAGE ANALYSIS

S. Hinz[1], M. Stephani[2], L. Schiemann[3], F. Rist[3]

[1]Remote Sensing Technology
[2]Photogrammetry and Remote Sensing
[3]Institute of Structural Design
Technische Universität München, Arcisstr. 21, 80 333 München, Germany
{Stefan.Hinz | Manfred.Stephani}@bv.tum.de; L.Schiemann@lrz.tum.de

KEY WORDS: ETFE-foils, close-range photogrammetry, shape reconstruction, bursting test, strain and stress behaviour

ABSTRACT:

The paper presents a modular photogrammetric recording and image analysis system for determining the 3D shape of **E**thylen-**T**etra**F**luor**E**thylen-Copolymer (ETFE) foils, including their evolution over time when put under increasing air pressure. Determining the time-variable 3D shape of transparent material imposes a number of challenges – especially, the automatic point transfer between stereo images and, in temporal domain, from one image pair to the next. We developed an automatic approach that accommodates for these particular circumstances and allows to precisely reconstructing the 3D shape for each epoch as well as determining 3D translation vectors between epochs by feature tracking. Examples including numerical results and accuracy measures prove the applicability of the system.

1. INTRODUCTION

The background of this work is a civil engineering project for testing new transparent construction materials – especially **E**thylen-**T**etra**F**luor**E**thylen-Copolymer (ETFE) foils. Membrane structures with ETFE-foils are used in building constructions in the last 25 years. Every year approximately 30 new famous ETFE-foils constructions are designed. The Allianz Arena in Munich and the Olympic Stadium Complex in Beijng for the Olympic Games 2008 are popular examples in which ETFE-foils are used for roof and facades structures. Recent projects of ETFE-foil structures show the tendency to increase the maximum span range for foil constructions. Therefore ETFE-foils are frequently stressed in the elastic range up to the yield stress or above it.

In general membrane materials are investigated with mono-axial and bi-axial tests. Bursting tests are adapted testing methods to analyze the material properties of ETFE in the viscoelastic and viscoplastic range up to the breaking point. They allow inspecting stress and strain behaviour of ETFE-foils with consideration of the rotationally symmetric deformation condition. This is one of the principal cases for pneumatic foil constructions (Moritz et al., 2005; Moritz, 2007). To test different material characteristics like stress and strain behaviour a low-cost measurement tool was set up that allows to produce densely sampled points with high accuracy in time and space domain. To this end, a photogrammetric close-range stereo system with specific image analysis software is an ideal tool. We outline the concept and realization of a modular photogrammetric recording and image analysis system for determining the 3D shape of ETFE-foils, including their evolution over time when put under increasing air pressure.

2. TEST SET-UP

In photogrammetric applications, textured and opaque materials need to be assumed in general. Both prerequisites are not met in our case. Hence, determining the time-variable 3D shape of transparent material imposes a number of challenges – most prominently, concerning the automatic point transfer from one stereo image pair to the next. To enable automatic matching of conjugate points, a black grid was printed onto each foil. Ideally, this grid would reflect some unique code to avoid ambiguous point matches caused by the grid's regularity. For this, however, specific printers or expensive projection hardware would have been necessary, which did not fit into the project's financial budget. Instead, a sophisticated matching strategy is incorporated, which is in particular able to cope with possible matching ambiguities.

Circular ETFE foil samples with a diameter of approx. 53 cm are clamped by a locking ring on a base plate. The foils are marked by grid lines. The cushions are inflated by means of electronically controlled pressure valves, while a digital pressure sensor measures the internal pressure in the cushion. Above the foil two digital high end user cameras are positioned. They record synchronously and automatically every five seconds the deformation of the ETFE-foil (see Fig. 1). Ultimately, the 3D position of grid crosses are determined by photogrammetric means and tracked over several stereo pairs (epochs). Hence, 3D translation vectors between each pair of epochs can be calculated.

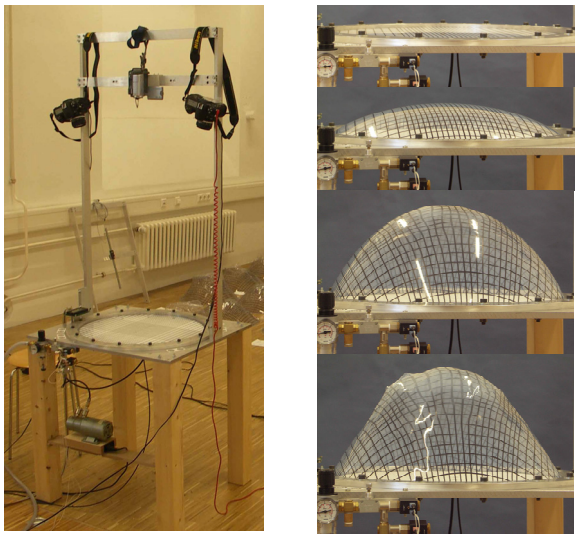

Fig.1: Experimental set-up and bursting test

3. IMAGE ANALYSIS SYSTEM

The overall processing scheme consists of following steps:

3.1 Camera calibration:

The two digital cameras of type Nikon D200 (3872 x 2592 Pixels of 6.096 micron size, corresponding to 23.6 mm x 15.8 mm image size) used are equipped with off-the-shelf 24 mm lenses. In order to exploit their full accuracy potential, calibration of the cameras in a similar environment as in our set up is a prerequisite. The parameters of inner orientation (incl. distortion parameters) of the two cameras were determined offline using a 3D test field with known ground control points. With each of the cameras 8 images of the test field where used to derive the calibrated focal length, the coordinates of the principal point and two parameters describing the distortion of the lenses. In order to obtain precise and reliable interior orientation parameters sub-pixel image measurements are desirable and the redundancy of the least squares adjustment should be as high as possible. Main results of the calibration procedure are presented in Table 1.

Parameter	Camera 1	Camera 2
Focal length [mm]	24.590	24.610
Principal point x [mm]	+0.063	-0.010
Principal point y [mm]	+0.012	+0.091
Distortion coeff. A1 [m^{-2}]	-154.9295	-157.7906
Distortion coeff. A2 [m^{-4}]	+245041.5	+257126.5
Sigma naught [micron]	1.7	1.8
Redundancy	464	466

Tab.1. Camera calibration results

3.2 Relative and absolute camera orientation

Various circular markers with known "real-world" co-ordinates have been placed in the vicinity of the ring (see Fig. 2a). These markers are automatically detected in and matched over the images. To this end, we adapted the shape-based matching algorithm proposed by (Steger, 2001) and (Ulrich, 2003).

A gradient filter is applied to the template image (Fig. 2b) and the gradient directions of each pixel are determined. The same is done for the search images. For determining the best matches, the template image is shifted over the search image and, for each position, the gradient directions of template and search image are compared. A similarity measure is calculated defined as the average vector product of the gradient directions of the template and the search image. This similarity measure is invariant against noise and illumination changes but not against rotations and scale. Hence the search must be extended to a predefined range of rotations and scales, which can be easily derived from approximate values given by the test set-up. Since we know the number N of markers, we can simply restrict the search to the N best matches. The matches are further refined to sub-pixel accuracy by fitting a second-order polynomial to the found matching parameters in a small neighborhood in parameter space.

Figure 2c) shows the final accuracy of the derived center coordinates and Fig. 3 illustrates the shape-based matching procedure. The final orientation of both cameras is then determined through bundle adjustment (see (Mikhail et al., 2001) for details).

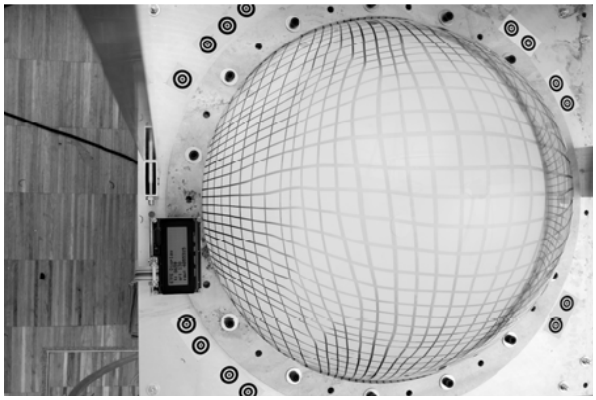

(a) Markers in vicinity of ring

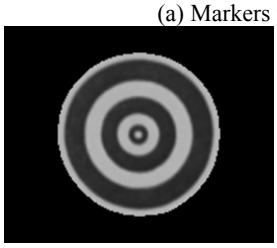

(b) Template

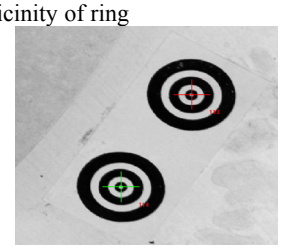

(c) Derived center coordinates

Fig.2. Automatic detection of markers

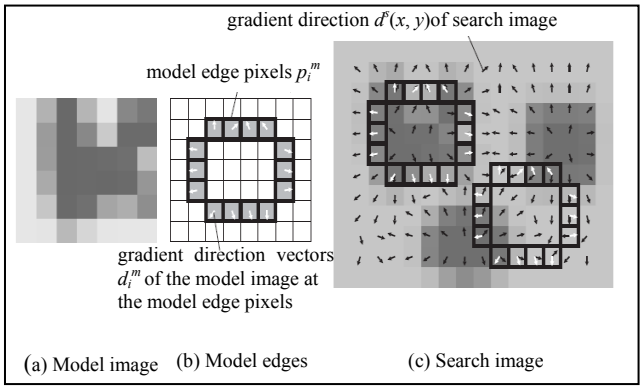

Fig. 3. Principle of the shape-based matching method, taken from (Ulrich, 2003), p. 70

3.3 Initial extraction and matching of features

In the initial (flat) state of the foil, more constraints can be incorporated into feature extraction and feature matching. Hence, this step is separated from the others. It consists of:

3.2.1 Point extraction: The crossings of the grid are determined by extracting dark lines using the approach of Steger (1998) and intersecting the endpoints and junction points of these lines. The positions of the resulting intersections are further refined by fitting a second order 2D polynomial to the grey values yielding eventually sub-pixel precision (see Fig.4).

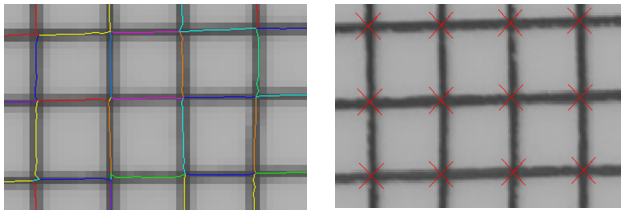

Fig. 4. Line extraction (left) and refined junction points (right)

3.2.2 Initial point matching: In the next step, conjugate feature points are determined in both images. Since the foil is flat in its initial state, a homography provides a sufficient mathematical model for point transfer and prevents a wrong solution due to over-parameterization and potential ambiguous matches. Furthermore, the search space for conjugate features can be significantly reduced in image space, since the feature points on the foil are almost co-planar with the already reconstructed 3D points of the markers. The point transfer is then calculated by estimating the parameters of the homography while maximizing the number of point correspondences using a RANSAC search algorithm, thereby the initial parameter values being derived from the camera orientation and test set-up. The optimization measure is computed from the number of points ("RANSAC inliers"), the accuracy of the estimated homography parameters and the grayvalue similarity of a small patch around the feature points. After having found a reasonably good solution through RANSAC, triangulating the resulting conjugate points yields their final 3D position in object space. Figure 5 depicts a detailed view on the resulting conjugate points.

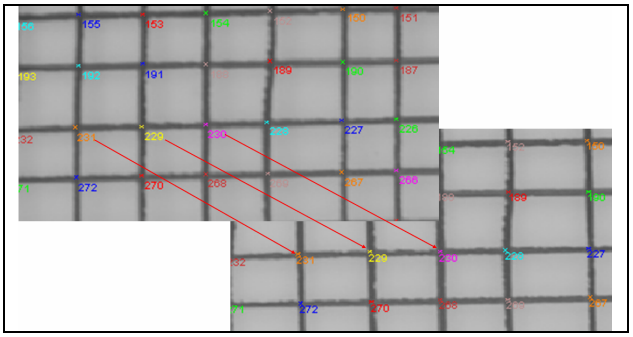

Fig. 5. Result of point transfer based on a homography

3.4 Iterative point tracking

It seems straightforward to apply the above procedure to each image pair of the sequence. However, once the foil expands, a larger search space and a less stringent mathematical model for point transfer needs to be incorporated, which – in turn – may result in more ambiguous matches. In addition, the deformation of the foil leads to a significant dissimilarity of the grayvalue patches of conjugate points when seen from the two camera position. To circumvent these problems, an alternative procedure has been implemented:

The conjugate points of the first epoch (t = 0) are tracked over the next epochs (t = 1…n) separately for the images of each camera (see Fig. 6 for illustration). To this end, a small patch around each point is selected and – similarly to pyramid tracking – matched to a search area of the image of the next epoch. Here, the image patch is updated and matched to the following epoch. Updating the image patch is necessary to accommodate the increasing deformation of the grid from epoch to epoch, see e.g. Fig. 7 that shows the result of point tracking in a later epoch. Tracking a particular point aborts when no reliable match can be established.

Please notice that, in this step, it is not necessary to search for corresponding points in the left and right image. The correspondences have been established in the initial matching step and are simply kept during point tracking via point indexing.

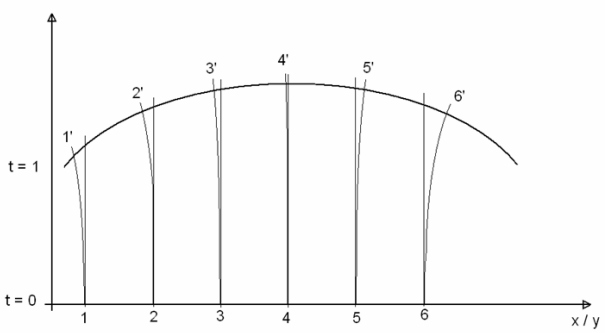

Fig. 6. Illustration of point tracking algorithm

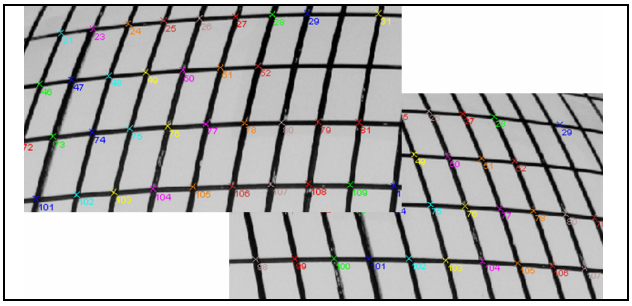

Fig. 7. Matched points in later epoch

3.5 Bundle adjustment

Bundle adjustment is considered the most appropriate tool to calculate 3D-object coordinates from multiple image coordinate measurements (Mikhail et al., 2001). The image coordinates and control point coordinates are introduced as observations into the least square adjustment process, while the exterior orientation (position and attitude) of the images and the object coordinates of homologues points are the unknowns to estimate. The interior orientation of the cameras is considered as given from the calibration process.

For relating all relevant parameters, the following well-known relation applies:

$$\begin{bmatrix} x'-x_0'-dx' \\ y'-y_0'-dy' \\ -c \end{bmatrix} = \frac{1}{m} \begin{bmatrix} r_{11} & r_{21} & r_{31} \\ r_{12} & r_{22} & r_{32} \\ r_{13} & r_{23} & r_{33} \end{bmatrix} \cdot \begin{bmatrix} X-X_0 \\ Y-Y_0 \\ Z-Z_0 \end{bmatrix}$$

where:

x',y'	measured image coordinates
x_0',y_0'	principal point coordinates
c	focal length
dx', dy'	distortion corrections
m	scale factor
r_{ik}	rotation matrix elements
X,Y,Z	object coordinates
X_0,Y_0,Z_0	projection centre

The scale factor can be eliminated through dividing the first and second line of the equation above by the third line. Then, one obtains two highly nonlinear observation equations for each image point:

$$x' + v_{x'} = x_0' - c \cdot \frac{r_{11}(X - X_0) + r_{21}(Y - Y_0) + r_{31}(Z - Z_0)}{r_{13}(X - X_0) + r_{23}(Y - Y_0) + r_{33}(Z - Z_0)} + dx'$$

$$y' + v_{y'} = y_0' - c \cdot \frac{r_{11}(X - X_0) + r_{21}(Y - Y_0) + r_{31}(Z - Z_0)}{r_{13}(X - X_0) + r_{23}(Y - Y_0) + r_{33}(Z - Z_0)} + dy'$$

where:

$v_{x'}, v_{y'}$ corrections to the image coordinates x',y'

dx', dy' radial distortion corrections

The radial distortion dr'

$$dr' = A_1 \left(r^3 - r \cdot r_0^2 \right) + A_2 \left(r^5 - r \cdot r_0^4 \right)$$

is split-up in two components dx' and dy' (first and second term), where r is the distance to the centre (radius), r_0 the reference radius and A_1 and A_2 the distortion coefficients obtained from the calibration procedure.

Thus, for each coordinate triple X, Y, Z of an object point to be calculated, four observations (image coordinates, two in each image) are available. As all coordinates of the markers are considered as error-free ground control information, the resulting redundancy of the bundle adjustment increases with increasing number of ground control points and object points to be determined. In order to keep the number of iterations low, suitable initial values for all unknowns are calculated at the beginning of the least squares adjustment process. Typically 650 to 880 object points are calculated iteratively by an optimized intersection of spatial rays (extended bundle adjustment) from each image pair (epoch).

The final 3D co-ordinates of each epoch's points including their accuracy and point IDs are stored to allow the computation of time-dependent 3D translation vectors between points of various epochs. The result of 3D point determination of an intermediate epoch is shown in Fig 8.

3.6 Surface Generation

The deformations of the foils are tracked through the adjusted 3D coordinates for each epoch of the points marked on the surface of the foils. Hence the behaviour of the foil can be studied and deformation parameters (strain, curvature etc) derived. On the other side these more or less arbitrary distributed 3D points for each epoch can be used to calculate a regularly grided surface using the Golden Software Package "Surfer 8". Afterwards different visualizations of the shape of the inflated foils are feasible.

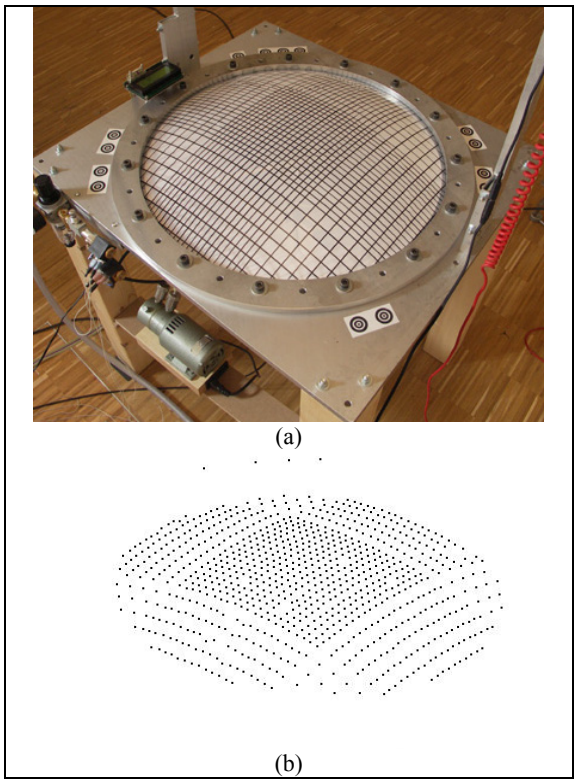

(a)

(b)

Fig. 8. 3D point determination in intermediate epoch: (a) current state of foil, (b) reconstructed 3D points.

4. RESULTS

With the coordinates of the matching points three-dimensional scatterplots of the deformed geometry of the ETFE cushions are determined (cf. Figs. 9, 10). They show the deformed geometry of the foil at each epoch due to the internal pressure. For the epoch shown in Fig. 10, the maximum vertical deformation of the circular ETFE-foil samples is 27,425 cm. At the beginning of the test the scatterplot exists of approx. 1000 points, while. the finite element net exists of approx. 850 4-nodes elements. The curvature of the deformed geometry

$$\kappa = \frac{f''(x)}{(1 + f'(x)^2)^{3/2}}$$

is calculated from the deformation function *f(x)* of the foils at each epoch.

To observe and describe how the foils deform during the inflating process differential geometry and continuums mechanics basics are applied to the points tracked over epochs. The Green-Lagrange-strain tensor

$$E = \tfrac{1}{2}(g_{ij} - G^{ij})\, G^i \otimes G^j$$

describes the mechanical behaviour of the foils in consideration of the nonlinear strain measures and the large deformation. E is calculated with the difference of the metric coefficients. The covariant metric tensor g_{ij} from the local covariant basis describes the metric of the surface for the reference geometry at time t_o. The metric of the surface at each epoch at time t_i is described with the contravariant metric tensor G^{ij}. Figures 11a-d) show a typical example after a 195 seconds inflation period and an internal pressure of 30900 Pa. The strains are depicted in addition to the deformed foil, the scatterplot and the shaded relief map.

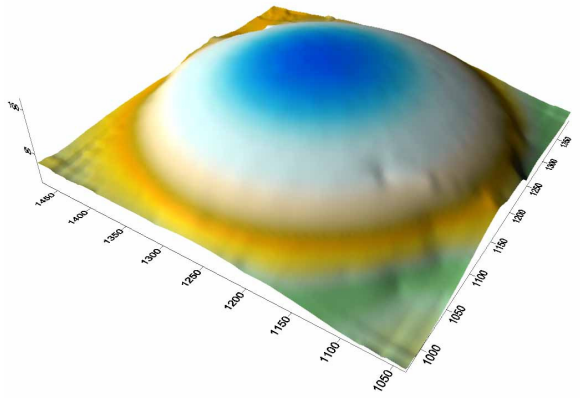

Fig. 9. Visualization of interpolated surface

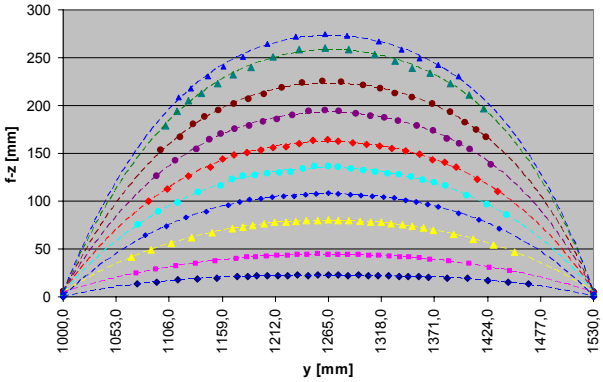

Fig 10. Deformation of the cushion for different pressures

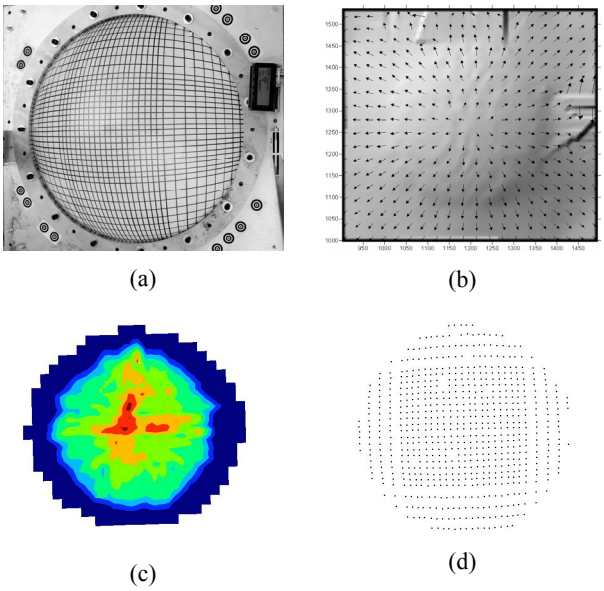

(a) (b)

(c) (d)

Fig. 11: Results, time t=195s, p_i = 30900Pa, (a) deformed foil, (b) shaded relief map, (c) strains and (d) scatterplot

5. CONCLUSION

The results from the photogrammetric image analysis show that, despite of the challenging environment, an average point accuracy of 1/3 pixel at image scale could be reached. In addition, the point density (starting with 100%) remains high for approx. ¾ of the tracked image pairs and drops down, due to increasing occlusions, to the end of tracking, only.

It must be pointed out that for the accurate calculation of the nonlinear strain measures a high point accuracy of the determination of the grid point coordinates is necessary. In our case the large deformation and the transparent material complicate the determination of the points. The achieved point accuracy of 1/3 pixel at image scale enable an accurate determination of the deformations and of the curvatures. The calculated results are adequate to investigate qualitatively the strain behaviour of the foils. However, the point accuracy must be improved to calculate accurately the strains. Possible improvements are smoothing the surface, fitting the point coordinates, using a third camera or increasing the inclination of the cameras.

The developed bursting test including the photogrammetric recording and image analysis system is a possibility to investigate transparent materials, like ETFE-foil, in the viscolelastic range up to the breaking point. In addition to the determination of the deformation and curvature, the tests analyse the breaking behaviour of circular ETFE-foil cushions.

REFERENCES

Mikhail, E., Bethel, J., McGlone, C., 2001. Introduction to Modern Photogrammetry. John Wiley & Sons.

Moritz, K., Brengelmann, T., Schiemann, L., 2005. Steel Service Station Roofs with Plastic Membranes, DETAIL 7/8.

Moritz, K., 2007. Bauweise der ETFE-Foliensysteme, Stahlbau 76 (5)

Steger, C., 1998. An unbiased detector of curvilinear structures, *IEEE Trans. Pattern Anal. Machine Intell.,* 20(2), pp. 549-556.

Steger, C. (2001): Similarity measures for occlusion, clutter, and illumination invariant object recognition. In: B. Radig and S. Florczyk (eds.) *Pattern Recognition,* DAGM 2001, LNCS 2191, Springer Verlag, 148–154.

Ulrich, M., 2003. Hierarchical Real-Time Recognition of Compound Objects in Images. Dissertation, German Geodetic Commission (DGK), Vol. C.